Nanoporous Hollow Transition Metal Chalcogenide Nanosheets Synthesized *via* the Anion-Exchange Reaction of Metal Hydroxides with Chalcogenide Ions

Weiwei Zhao, Chao Zhang, Feiyang Geng, Sifei Zhuo, and Bin Zhang*

Department of Chemistry, School of Science, Tianjin University, and Collaborative Innovation Center of Chemical Science and Engineering (Tianjin), Tianjin 300072, China

ABSTRACT Nanoporous hollow transition metal chalcogenides are of special interest for a variety of promising applications. Although some advanced synthetic methods have been reported, the development of a facile and general strategy to fabricate porous hollow nanostructures of transition metal chalcogenides, especially with enhanced electrocatalytic performance, still remains highly challenged. Herein, we report a facile chemical transformation strategy to prepare nanoporous hollow Co_3S_4 nanosheets *via* the anion exchange reaction of $Co(OH)_2$ with sulfide ions. The chemical transformation mechanism involves the as-formed layer of nanoporous cobalt sulfide on $Co(OH)_2$ driven by the anion-exchange-reaction and lattice mismatch induced quick strain release, a following diffusion-effect-dominated core–shell hollow intermediate with hollow interiors, and subsequent Ostwald ripening growth of hollow nanosheets at elevated temperatures. This anion-exchange strategy of transition metal hydroxides with chalcogenide ions is also suitable for fabricating nanoporous hollow nanosheets of other metal chalcogenides (*e.g.*, $CoSe_2$, $CoTe_2$, CdS, and NiS). The as-prepared nanoporous hollow Co_3S_4 nanosheets are found to be highly active and stable for electrocatalytic oxygen evolution reaction.

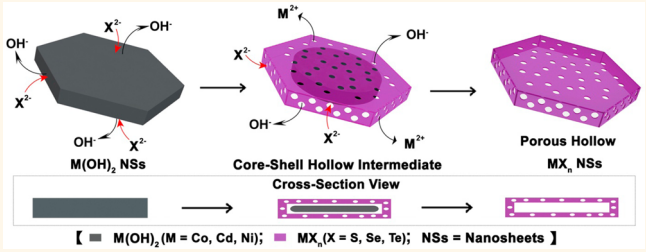

KEYWORDS: anion exchange · metal chalcogenides · metal hydroxides · mesoporous · nanostructures

Intriguing applications of transition metal chalcogenide nanostructures in catalysis, solar cells, lasers, batteries, and thermoelectrics are driving the exploration of synthetic method to manipulate their chemical composition, morphology and structure.[1−9] Recently, porous nanostructures have received increasing attention for their improved physical and chemical properties in comparison with their solid nanoscale counterparts.[10−13] Hollow nanostructures with well-defined cavities have been employed in many fields due to the merits of low density, large specific surface area, and large void space.[14−17] In particular, two-dimensional nanostructures with cavities have possessed novel properties because of their unique geometrical configuration, which is different from zero- and one-dimensional nanostructures.[18−20] Although some advanced achievements have been made in the synthesis of metal chalcogenides,[2,21−25] the preparation of nanoporous hollow two-dimensional nanostructure of metal chalcogenides remains unexplored. Thus, it is highly desirable to develop a generalized and efficient strategy to synthesize nanoporous hollow nanosheets of transition metal chalcogenides.

Since the first report of cation exchange reaction in inorganic nanocrystals by Alivisatos and his co-workers,[26] ion-exchange reaction has been considered to be one of the most important chemical transformation methods to adjust the composition, structure and properties.[27−37] For instance, Jeong and his co-workers have carried out a well-designed ion-exchange reaction in generating diverse ultrathin chalcogenide nanowires M_xTe_y (M = Cd, Zn, Pb, and Pt).[27]

* Address correspondence to bzhang@tju.edu.cn.

Received for review August 24, 2014 and accepted October 5, 2014.

Published online October 06, 2014
10.1021/nn504755x

The facile preparation of solid nanocrystals has been achieved through cation exchange reaction of metal sulfide and telluride nanocrystals by the Manna and Moreels groups.[28,29] Schaak *et al.* have reported an efficient anion exchange pathway to convert colloidal metal selenides to the corresponding metal tellurides.[30] Very recently, we have demonstrated the ion-exchange method of inorganic–organic hybrid nanostructures to obtain nanoporous metal sulfide and selenides.[38,39] But the synthesis of inorganic–organic precursors always utilizes either high temperature or toxic solvents with a relatively complicated process.[3,38,39] Therefore, the search of a satisfactory alternative material to hybrid precursors is significant in producing nanoporous nanomaterials *via* the ion-exchange way. Furthermore, the development of a generalized ion-exchange strategy to fabricate nanoporous hollow metal chalcogenide nanostructures, especially with improved electrocatalytic performance, still remains a great challenge.

Herein, we present a facile and generalized anion exchange strategy of transition metal hydroxides with chalcogenide ions to produce nanoporous hollow nanosheets of transition metal chalcogenides under mild hydrothermal conditions. Cobalt sulfide is selected as the mode target because of its promising candidate as earth-abundant and inexpensive energy conversion and storage materials.[40−42] By the anion exchange reaction of easy-prepared inorganic $Co(OH)_2$ nanosheets with thioacetamide, nanoporous hollow cobalt sulfide nanosheets are successfully fabricated with the retention of macro-sized sheet-like morphology (Figure 1a). Moreover, this anion exchange strategy of metal hydroxide materials is suitable for the fabrication of other nanoporous hollow transition metal chalcogenide nanostructures, such as, nanoporous hollow $CoSe_2$, $CoTe_2$, CdS, and NiS nanosheets. The difference in solubility between reactants and products ($K_{sp(M(OH)2)} > K_{spMXn(X=S,Se,Te)}$ in Supporting Information Table S1) determines that the anion-exchange reaction from transition metal hydroxides to metal chalcogenides is favorable under the impetus of thermodynamic driving force.[27,43,44] Furthermore, the as-prepared nanoporous hollow cobalt sulfide nanosheets display high electrochemical oxygen evolution reaction (OER) activity and stability in alkaline medium, making them promising inexpensive electrocatalysts for oxygen production.

RESULTS AND DISCUSSION

The starting inorganic $Co(OH)_2$ nanosheets are fabricated by a facile hydrothermal method reported by Qiu and co-workers.[45] The as-prepared products are first characterized by scanning electron microscopy (SEM), transmission electron microscopy (TEM), and X-ray diffraction (XRD). The SEM image (Figure 1b) and TEM image (Supporting Information Figure S1) clearly show that solid $Co(OH)_2$ nanosheets are successfully fabricated in large quantities. Typical powder X-ray diffraction (XRD) pattern displayed in Figure 1j identifies these hexagonal sheets as hexagonal $Co(OH)_2$ (JCPDS No. 30-0443). For a typical anion-exchange reaction, an aqueous solution with the $Co(OH)_2$ hexagonal

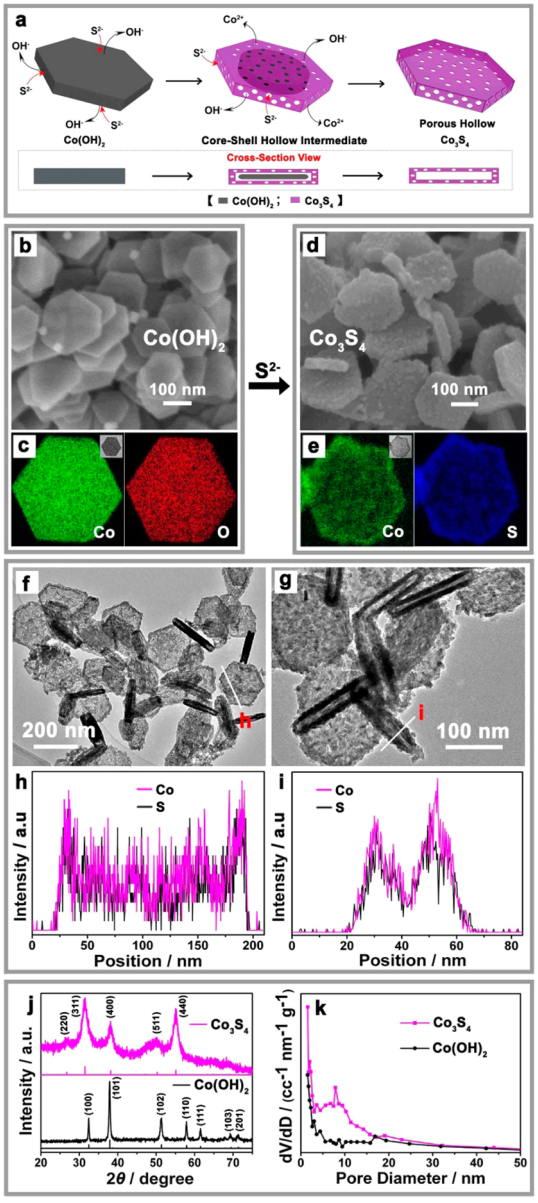

Figure 1. Preparation of nanoporous hollow Co_3S_4 nanosheets *via* the anion-exchange reaction of $Co(OH)_2$ with sulfide ions. (a) Schematic illustrations of the chemical transformation mechanism of nanoporous hollow Co_3S_4 nanosheets, which is prepared by the anion-exchange reaction of $Co(OH)_2$ with sulfide ions. (b) SEM image and (c) EELS elemental mapping images of the starting $Co(OH)_2$ nanosheets. (d) SEM image, (e) EELS mapping elemental image, (f and g) TEM images of the as-converted nanoporous hollow Co_3S_4 sheets. (h) Front-view and (i) side-view EDS line-scan elemental distributions of one typical nanoporous hollow Co_3S_4 nanosheet. (j) XRD patterns and (k) mesopore size distributions of the starting $Co(OH)_2$ nanosheets and the as-converted nanoporous hollow Co_3S_4 sheets.

nanosheets (Figure 1b) as precursors and excessive thioacetamide as sulfur source is hydrothermally treated at 120 °C for 6 h. Upon the anion-exchange reaction, solid sheets become nanoporous hollow products (Figure 1d–g). The SEM (Figure 1d) and TEM images (Figure 1f,g) reveal that nanopores are obviously observed throughout the nanosheets and the sheet-like morphology remains unchanged after the transformation is completely performed. Mesopore size distributions (Figure 1k) and mesopore nitrogen adsorption/desorption isotherms (Supporting Information Figure S2) suggest that the average pore size and surface area of the as-converted nanoporous hollow nanosheets are 7.9 nm and 74.1 m^2/g, respectively. The anion-exchange reaction is further characterized using electron energy loss spectroscopic (EELS) elemental mapping. As shown in Figure 1c, Co and O elements are uniformly distributed in a starting solid hexagonal $Co(OH)_2$ nanosheet. After the $Co(OH)_2$ nanosheets are hydrothermally treated with thioacetamide, the EELS images in Figure 1e indicate the uniform distribution of Co and S, illustrating the transformation from the transition metal hydroxides into metal sulfides. The point-scan energy-dispersion X-ray spectrum (EDS) (Supporting Information Figure S3) also confirms that the as-transformed porous products are only composed of Co and S. The typical front-view line-scan EDS profile of a single cobalt sulfide nanosheet (Figure 1h) clearly displays that the signals of Co and S elements in the edge of the nanoporous sheets are higher than those in the interior regions, suggesting the hollow structure of the as-obtained samples. The bimodal distribution of Co and S in the representative side-view line-scan EDS profile (Figure 1i) further reveals the unique hollow character of the as-converted cobalt sulfide nanosheets. The crystal structure and phase composition of the nanoporous hollow products are characterized using X-ray powder diffraction (XRD). All diffraction peaks in this XRD pattern (Figure 1j) can be indexed to the cubic Co_3S_4 (JCPDS No. 47-1738). It is found that the calculated crystallite size using Scherrer formula on the basis of the (311) diffraction peak of XRD pattern is 10.2 nm, which is consistent with the size of about 10 nm observed in TEM image (Figure 1g). X-photoelectron spectroscopy (XPS) analysis evaluates the chemical bonding states of each element on the surface of the Co_3S_4 sample (Supporting Information Figure S4). The core level spectrum of Co 2p region is deconvoluted into two spin–orbit doublets. The first doublet at 778.9 and 796.3 eV and the second at 780.4 and 800.0 eV are attributed to Co^{3+} and Co^{2+}, respectively. In the core level spectrum of S 2p region, the binding energies at 161.6 and 162.5 eV are assigned to S $2p_{3/2}$ and S $2p_{1/2}$, respectively. These results are in good agreement with the reported values.[46] The morphology and structure of the nanoporous hollow Co_3S_4 nanosheets are further characterized using high-resolution TEM (HRTEM) and selected area electron diffraction (SAED). The HRTEM image and SAED pattern (Supporting Information Figure S5) further show that the as-converted nanoporous hollow Co_3S_4 products are polycrystalline nanosheets composed of highly crystalline nanoparticles. The crystal structural sketch further highlights the replacement of the anion sublattice of hexagonal $Co(OH)_2$, such that OH^- ion is replaced by S^{2-} ion, and yields a cubic Co_3S_4 lattice through the anion-exchange of the $Co(OH)_2$ with S^{2-} (Supporting Information Figure S6). These results clearly demonstrate that the inorganic solid $Co(OH)_2$ hexagonal nanosheets can be completely converted into nanoporous hollow Co_3S_4 nanosheets with the retention of the 2D macroscopic morphology *via* an anion-exchange reaction.

To get insight into the chemical transformation mechanism of nanoporous hollow Co_3S_4 nanosheet prepared by the anion-exchange reaction method, TEM, XRD and line-scan EDS elemental distributions are adopted to characterize the intermediates collected at different reaction stages. As shown in Figure 2a,e, the Co element is uniformly distributed in a starting solid $Co(OH)_2$ sheet. When the exchange reaction of the $Co(OH)_2$ nanosheets with thioacetamide at 120 °C proceeds for 0.5 h, the sheets become rough and a few of nanopores appear on their surface (Figure 2b and Supporting Information Figure S7). The associated XRD pattern (Figure 3) shows that the intermediates collected at 0.5 h are composed of unreacted $Co(OH)_2$ and as-converted Co_3S_4, thus confirming that $Co(OH)_2$ in the starting materials is partially converted into Co_3S_4. These results suggest that S^{2-}, produced by the thermal decomposition of thioacetamide, quickly exchanges with OH^- anions of $Co(OH)_2$ to form a thin layer of cobalt sulfide at the surface of the starting metal hydroxide nanosheets. The lattice mismatch between $Co(OH)_2$ and Co_3S_4 (Supporting Information Table S2) can cause the quick strain release and lead to the appearance of nanopores. Similar strain-driven formation of pores has been observed and theoretically predicted for cation exchange reaction of nanocrystals.[47−50] Despite of the existence of some nanopores on the as-formed Co_3S_4 layer, the Co_3S_4 layer still restricts, to some extent, the exchange reaction of outside sulfide ions with inner OH^- ions and the direct reaction with cobalt ions. In the following process, since the outward diffusion of cobalt cations becomes dominant in comparison with the inward diffusion of sulfide ions,[21,51] the Kirkendall effect can lead to the generation of hollow nanosheet with a visible $Co(OH)_2$ core.[52] At the same time, the presence of pores on the Co_3S_4 layer enables some sulfide ions to diffuse inward and react with the $Co(OH)_2$ core, which leads the partial transformation of $Co(OH)_2$ core into Co_3S_4 (Supporting Information Figure S8). This assumption is proved to be reasonable by the appearance of core–shell hollow

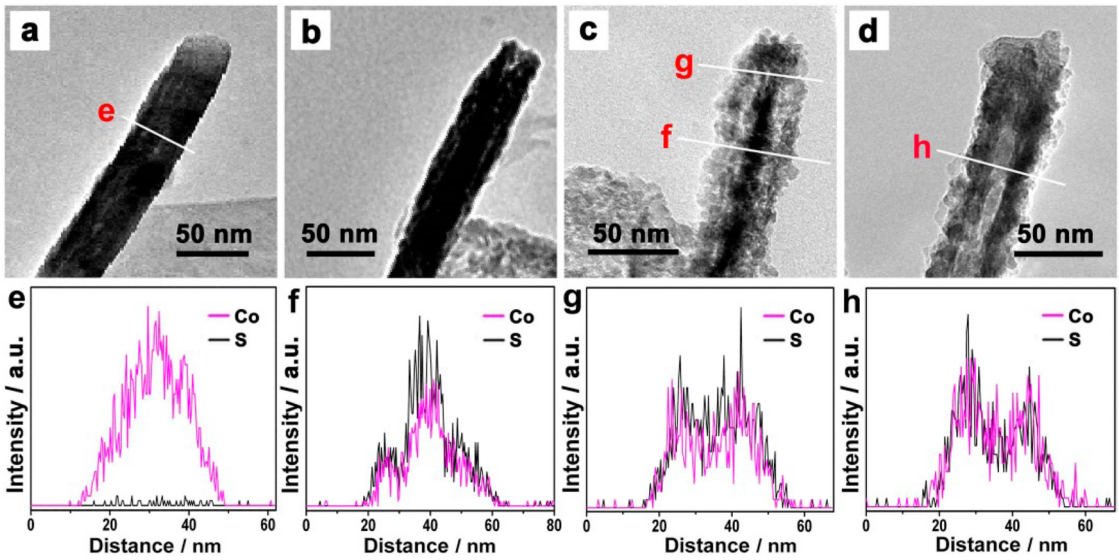

Figure 2. (a–d) Side-view TEM images and (e–h) line-scan EDS elemental distributions of the representative intermediates collected after the anion-exchange reaction proceeded for 0 h (a and e), 0.5 h (b), 2 h (c, f, and g) and 4 h (d and h).

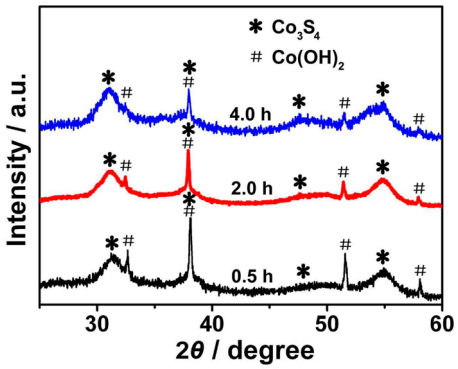

Figure 3. XRD patterns of the intermediates collected at 0.5 h (black line), 2 h (red line), and 4 h (blue line).

intermediate collected at 2 h (Figure 2c,f,g). The typical TEM image shows the core–shell hollow structure of the intermediate (Figure 2c). The corresponding EDS line-scan elemental distributions confirm that the core is Co_3S_4-rich (the three-peak distribution of Co and S in Figure 2f) and the shell is nanoporous Co_3S_4 (the bimodal distribution of Co and S in Figure 2g) in the hollow intermediate. In the corresponding XRD pattern of the intermediates at 2 h (Figure 3), the diffraction peaks of $Co(OH)_2$ decrease but the Co_3S_4 peaks increase during chemical transformation, indicating the continuous transformation of $Co(OH)_2$ to Co_3S_4. When the anion-exchange reaction is prolonged to 4 h, the detectable reflection peaks of the XRD pattern are predominantly indexed to cubic Co_3S_4, but still containing small parts of $Co(OH)_2$ (Figure 3). The signal intensity of the Co and S in the side-view central position of the line-scan EDS profiles becomes very weak and the bimodal distribution of Co and S gradually appears (Figure 2d,h). This result suggests that the Co_3S_4-rich core gradually disappears and the hollow interiors are becoming more and more obvious, which may be associated with the Ostwald ripening process.[53,54] The further prolonged transformation reaction time leads to a more obvious bimodal distribution of Co and S (Figure 1i), and finally generates nanoporous hollow Co_3S_4 nanosheets. On the basis of these above-mentioned results, the chemical transformation mechanism involves the as-formed layer of nanoporous cobalt sulfide on $Co(OH)_2$ driven by the anion-exchange-reaction and lattice mismatch induced quick strain release, a following diffusion-effect-dominated hollow core–shell intermediate with hollow interiors, and subsequent Ostwald ripening growth of hollow nanosheets at elevated temperatures.

The effects of the concentration and temperature on this anion-exchange reaction are investigated. In control experiments, when thioacetamide concentration of 3.5 mg/mL is adopted (that is, the mole ratio of Co in $Co(OH)_2$ and S in thioacetamide is 1:10), the starting $Co(OH)_2$ precursors can be fully converted into nanoporous hollow Co_3S_4 nanosheets at 6 h (Figure 1). When the concentration of thioacetamide is decreased to 1.4 and 0.6 mg/mL, the starting $Co(OH)_2$ are partially converted into cubic Co_3S_4 at 6 h (Supporting Information Figure S9b,d). The fully converted nanoporous hollow Co_3S_4 nanosheets are obtained when the reaction time is increased to 12 h (Supporting Information Figure S9). These results display that the concentrations do exert an important effect on the anion-exchange reaction of $Co(OH)_2$ with S^{2-}. An increasing concentration of sulfur source can effectively accelerate the anion-exchange reaction velocity. When the reaction temperature is set as 90 or 160 °C, nanoporous Co_3S_4 nanosheets can be also prepared, while the hollow space of the nanoporous Co_3S_4 nanosheets becomes much smaller at a higher temperature

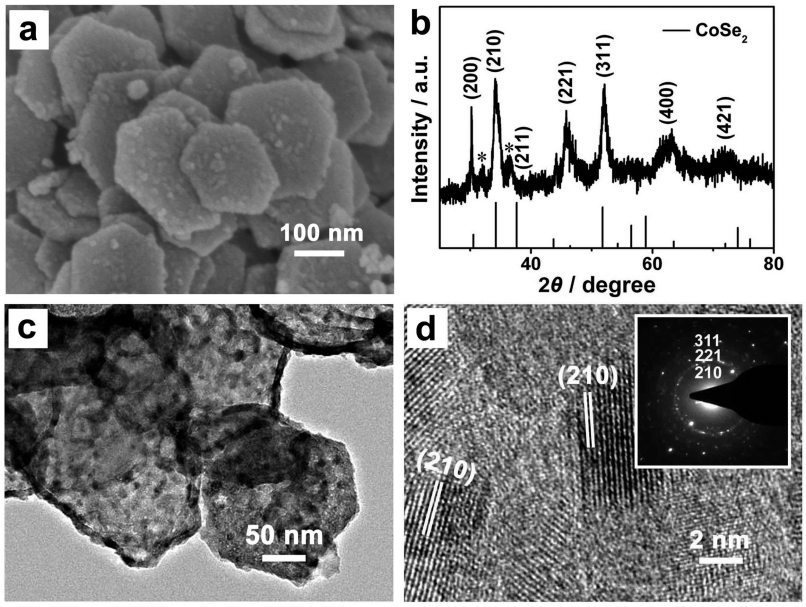

Figure 4. Structural characterizations of the nanoporous hollow $CoSe_2$ nanosheets prepared *via* the anion-exchange conversion of $Co(OH)_2$ nanosheets with selenium ions. (a) SEM image, (b) XRD pattern, (c) TEM image, and (d) HRTEM image and SAED pattern (the inset of d) of the nanoporous hollow $CoSe_2$ nanosheets. Two weak peaks (*) in (b) are originated from unreacted Se powders.

(Supporting Information Figure S10a,b). It is mainly attributed to the fact that a higher temperature promotes quicker thermal decomposition of thioacetamide into S^{2-} ions and further accelerates the exchange rates of S^{2-} with OH^- anions of $Co(OH)_2$, thus forming a thicker layer of cobalt sulfide at the surface of the starting metal hydroxide nanosheets. Simultaneously, a higher temperature improves the adhesion between the $Co(OH)_2$ core and the Co_3S_4 shell.[21] The results indicate that an over-rapid anion-exchange rate of $Co(OH)_2$ and S^{2-} is helpless for the formation of nanoporous hollow structure *via* the anion-exchange reaction of $Co(OH)_2$ with S^{2-}. The conclusion is further supported by the fact that no obvious hollow region is observed in side-view TEM image of the as-converted Co_3S_4 samples obtained at 200 °C (Supporting Information Figure S10c). XRD patterns (Supporting Information Figure S10d) demonstrate that all the products are cubic Co_3S_4 phase (JCPDS No. 47-1738), displaying that the temperature (90−200 °C) has no effect on the crystal structure of as-transformed products in the anion-exchange reaction of $Co(OH)_2$ and S^{2-} ions. When NaHS is utilized as sulfur source, the products are also cubic Co_3S_4 (JCPDS No. 47-1738) structure, but no obvious nanoporous hollow structure is observed (Supporting Information Figure S11), which may be ascribed to the quick reaction between of NaHS and $Co(OH)_2$ weakening the role of the outward diffusion of OH^- ions in the $Co(OH)_2$ nanosheets. It further confirms that gradual and slow release of S^{2-} is vital for the formation of hollow structure and cubic Co_3S_4 is a thermodynamically stable phase in the transformation process.

Given the preliminary insights into the conversion mechanism from solid $Co(OH)_2$ to nanoporous hollow cobalt sulfide, the anion exchange transformation method of $Co(OH)_2$ should be applicable in the fabrication of metal selenides or tellurides. When solid powders of the $Co(OH)_2$ nanosheets are used as the starting materials for anion-exchange reactions with selenium ions[55,56] at an elevated temperature, nanoporous hollow cobalt selenide nanosheets can be generated (Figure 4). SEM image (Figure 4a) shows that the 2D macroscopic morphology of inorganic solid $Co(OH)_2$ hexagonal nanosheets is retained *via* the anion-exchange reaction of $Co(OH)_2$ nanosheets with selenium ions. As shown in the XRD pattern (Figure 4b), in addition of some peaks (*) of unreacted Se powders, all the detectable reflection peaks could be assigned to a cubic phase $CoSe_2$ with lattice constants of $a = b = c =$ 5.858 nm (JCPDS No. 09-0234). TEM image (Figure 4c) displays that the nanopores are obviously observed throughout the $CoSe_2$ nanosheets and the edge of the nanoporous sheets is thicker than the interior region, suggesting the hollow structure of the as-obtained samples. HRTEM image (Figure 4d) and SAED pattern (the inset of Figure 4d) show that the as-converted nanoporous hollow $CoSe_2$ nanosheets are polycrystalline, which are composed of highly crystalline nanoparticles. In the XPS spectra of nanoporous hollow $CoSe_2$ nanosheets, the peaks at 779.2, 794.1, and 55.30 eV can be attributed to the Co $2p_{3/2}$, Co $2p_{1/2}$, and Se $3d_{5/2}$, respectively (Supporting Information Figure S12).[57,58] When the amount of Se powders and $NaBH_4$ is decreased to 0.75 times than that in Figure 4, the as-obtained products are still nanoporous hollow

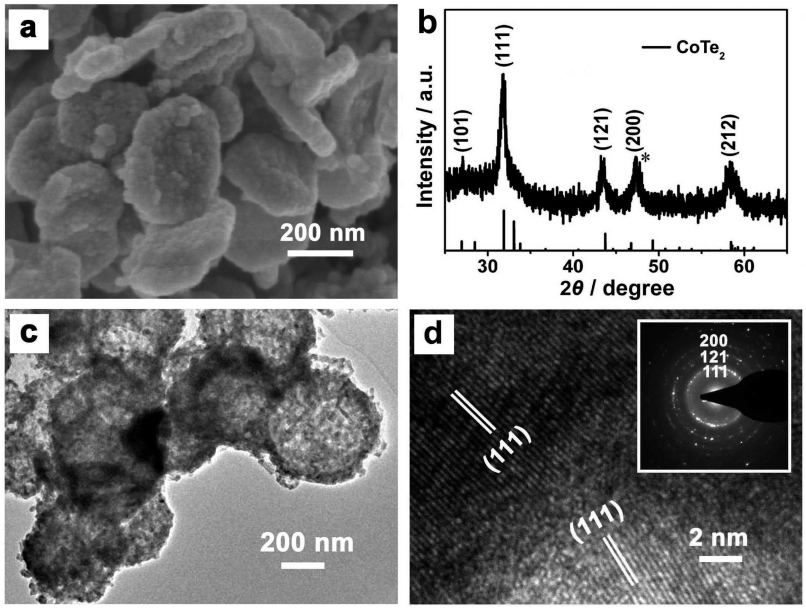

Figure 5. Structural characterizations of the nanoporous hollow $CoTe_2$ nanosheets prepared *via* the anion-exchange conversion of $Co(OH)_2$ nanosheets with tellurium ions. (a) SEM image, (b) XRD pattern, (c) TEM image, and (d) HRTEM image and SAED pattern (the inset of d) of the nanoporous hollow $CoTe_2$ nanosheets. One weak peak (*) in (b) is originated from unreacted Te powders.

$CoSe_2$ nanosheets (Supporting Information Figure S13). It shows that the anion-exchange reaction of $Co(OH)_2$ and selenium ions tends to form a stable pyrite $CoSe_2$ structure.[57,58] These results illustrate that this anion-exchange strategy of transition metal hydroxides can be considered as a generalized method to create nanoporous hollow nanostructures of metal selenides.

In addition, nanoporous hollow cobalt telluride nanosheets can also be obtained by using the same procedure. When solid powders of the $Co(OH)_2$ nanosheets are served as precursors for anion-exchange reactions with tellurium anions,[55,56] nanoporous hollow cobalt tellurides nanosheets can be obtained (Figure 5). As shown in Figure 5a, the sheet-like 2D macroscopic morphology remains unchanged after the anion-exchange reaction of $Co(OH)_2$ with tellurium ions is completely performed. XRD pattern (Figure 5b) is identified as orthorhombic phase $CoTe_2$ (JCPDS No. 74-0425) with lattice constants of a = 3.882 nm, b = 5.301 nm, and c = 6.298 nm. The typical TEM image (Figure 5c) clearly displays that $CoTe_2$ nanosheets are nanoporous and the edge is thicker than the interior region, suggesting that the nanoporous $CoTe_2$ nanosheets possess hollow structure. HRTEM image (Figure 5d) and SAED pattern (the inset of Figure 5d) display that the as-obtained nanoporous hollow $CoTe_2$ nanosheets are polycrystalline, which consist of highly crystalline nanoparticles. When the amount of Te powders and $NaBH_4$ is decreased to 0.75 times than that in Figure 5, the as-converted samples are still nanoporous hollow $CoTe_2$ nanosheets (Supporting Information Figure S14). It shows that the anion-exchange reaction of $Co(OH)_2$ and tellurium ions tends to form a stable pyrite $CoTe_2$ structure. The results demonstrate that this anion-exchange strategy of transition metal hydroxides can be considered as a general method to create nanoporous hollow nanostructures of metal tellurides with the retention of the macro-sized morphology.

The facile strategy presented here is also suitable for converting other solid inorganic transition metal hydroxides into nanoporous hollow metal sulfides. For instance, when single-crystalline $Cd(OH)_2$ nanosheets (Supporting Information Figure S15a,b) are used as starting materials and treated with thioacetamide, nanoporous hollow CdS nanosheets can also be produced (Supporting Information Figures S15c–h and S16). Additionally, the as-prepared nanosheet-based $Ni(OH)_2$ microspheres can also be transformed into NiS microspheres composed of nanoporous hollow nanosheets through an anion-exchange route in aqueous media (Supporting Information Figure S17). During these anion-exchange reactions, there are no dramatic changes of macro-sized morphology, which is important for rational synthesis of morphology-predicted porous hollow materials. These extending works indicate that our anion-exchange protocol of transition metal hydroxides may be developed into a generalized protocol for fabricating various nanoporous hollow metal sulfide nanostructures with the retention of the macro-sized morphology.

Recently, transition metal chalcogenides have been found to exhibit noble-metal-like electrocatalytic properties in the field of energy conversion and storage.[22,40–42,51,59–63] Here, the electrochemical oxygen evolution reaction (OER) is selected to evaluate the catalytic performance

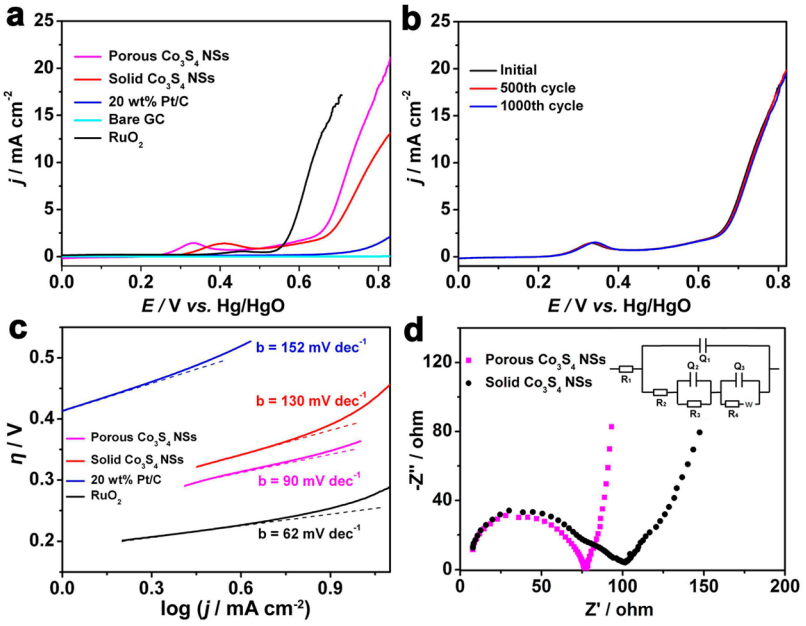

Figure 6. Electrochemical oxygen evolution reaction (OER) performance. (a) Polarization curves for OER on bare GC electrode and modified GC electrodes comprising the nanoporous hollow Co_3S_4 nanosheets (NSs), solid Co_3S_4 nanosheets synthesized by one-step approach, 20 wt % Pt/C, and RuO_2, respectively. (b) OER polarization curves for the nanoporous hollow Co_3S_4 nanosheets before and after different cycles of accelerated stability test. (c) Tafel plot (overpotential *versus* log current) derived from (a). (d) Electrochemical impedance spectroscopy of nanoporous hollow Co_3S_4 nanosheets and Co_3S_4 nanosheets synthesized by one-pot approach at η = 0.6 V. The inset shows the corresponding equivalent circuit. (Symbols R_1 and Q_1 represent the solution resistance and the total capacitance, respectively. R_2, R_3, and R_4 represent the charge transfer resistance, the contact resistance, and the diffusion resistance, respectively. Q_2, Q_3, and Q_4 are the corresponding capacitances.) Polarization curves are *iR*-compensated. The electrolyte: 0.1 M KOH. Scan rates: 10 mV s^{-1}.

for the as-obtained nanoporous hollow Co_3S_4 nanosheets. The as-synthesized solid Co_3S_4 nanosheets (Supporting Information Figure S18), commercial Pt/C (20 wt %, Johnson Matthey) and commercial RuO_2 (aladdin-reagent) with high OER catalytic performance are measured for comparison. The polarization curve ($j-V$ plot) (Figure 6a) shows that the nanoporous hollow Co_3S_4 nanosheets exhibit greater current density and lower onset potential of catalytic current as compared with solid Co_3S_4 nanosheets and commercial Pt/C. The potential required for the current density of 10 mA cm^{-2}, as a commonly used OER references and a metric relevant to solar fuel synthesis, is used to evaluate the OER activity. The nanoporous hollow Co_3S_4 nanosheets at 10 mA cm^{-2} achieve a small overpotential (η) of 0.363 V *vs* RHE (RHE: reversible hydrogen electrode), which is close to that of most efficient OER catalysts RuO_2 (0.266 V *vs* RHE), and superior to that of solid Co_3S_4 nanosheets (0.416 V *vs* RHE) and the best performance of the well-designed $NiCo_2S_4$@N/S-rGO catalysts at a same loading amount.[24] Corresponding Tafel plots (η-log j) (Figure 6c) are applied to estimate the OER kinetics of the above catalysts. The Tafel slope of nanoporous hollow Co_3S_4 nanosheets is 90 mV dec^{-1}, which is smaller than that of solid Co_3S_4 nanosheets. To evaluate the kinetics of electrode reactions, the electrochemical impedance spectroscopy (EIS) measurements are performed.[64,65] Figure 6d shows EIS spectra presented in Nyquist diagram in the frequency range of 1000 kHz to 20 mHz for nanoporous hollow Co_3S_4 nanosheets and solid Co_3S_4 nanosheets electrodes, which can be interpreted in terms of the equivalent circuit as shown in the inset of Figure 6d. It indicates that porous hollow Co_3S_4 nanosheets own a smaller charge transfer resistance (R_2 in the equivalent circuit) than that of solid Co_3S_4 nanosheets, demonstrating a much faster electron transfer process during electrochemical reaction.[66] The total capacitance (Q_1 in the equivalent circuit) of the porous hollow Co_3S_4 nanosheets is larger than that of solid Co_3S_4 nanosheets, indicative of a larger reaction specific surface area in the electrochemical reaction system.[67] This may be associated with much more active sites, improved ion conductivity and unique porous structure of the nanoporous hollow Co_3S_4 nanosheets.[68] In particular, the special porous hollow nanostructure is conducive to a fast diffusion and reaction at the electrolyte-electrode interface.[51] In addition, the accelerated stability tests are performed to further evaluate the stability of the nanoporous hollow Co_3S_4 nanosheets during electrocatalytic OER in 0.1 M KOH. Cyclic voltammetric (CV) sweeps between +0.3 and +0.8 V are applied to the nanoporous hollow Co_3S_4 nanosheets-decorated working electrode. After 1000 CV sweeps, the catalyst almost affords the same $j-V$ curve to the initial curve, demonstrating its excellent stability (Figure 6b).

CONCLUSIONS

In summary, we have reported a facile synthesis of nanoporous hollow Co_3S_4 nanosheets *via* the anion exchange reaction of $Co(OH)_2$ nanosheets with S^{2-} ions. The transformation mechanism of solid $Co(OH)_2$ into nanoporous hollow Co_3S_4 sheets seems to involve the quick anion-exchange reaction of the $Co(OH)_2$, the following diffusion effect and the subsequent Ostwald ripening process. The as-synthesized nanoporous hollow Co_3S_4 nanosheets exhibit high electrocatalytic activity and electrochemical stability toward OER, thus making them inexpensive candidates for oxygen production. In addition, the anion-exchange strategy of $Co(OH)_2$ nanosheets with chalcogenide ions is found to be successful in producing nanoporous hollow sheets of cobalt selenide and cobalt telluride. Furthermore, we demonstrate that the facile chemical transformation protocol can be broadened to convert other transition metal hydroxides into corresponding nanoporous hollow metal chalcogenide materials (*e.g.*, CdS, NiS) with well-preserved dimension and morphology. More importantly, these nanoporous hollow metal chalcogenides may find promising applications in various fields, such as OER, hydrogen evolution reaction, photocatalysis, batteries, lasers, supercapacitors and solar cells.

EXPERIMENTAL SECTION

Synthesis of Single-Crystalline Cobalt Hydroxide ($Co(OH)_2$) Nanosheets. The $Co(OH)_2$ nanosheets were synthesized using the reported method with a little modification.[45] In a typical procedure, $Co(NO_3)_2 \cdot 6H_2O$ (0.1091 g, 0.375 mmol) was dissolved into 15 mL of deionized water to form a pink solution at room temperature. Then, 0.375 mL of triethylamine was added dropwise to the mixed solution under magnetic stirring, and the solution immediately turned dark blue. Next, 14.625 mL of deionized water was added again to reach a total volume of 30 mL. The mixed solution was then transferred into a 50 mL Teflon-lined stainless-steel autoclave and kept at 180 °C for 24 h. The black samples were collected and washed several times with water and ethanol, separately, and then dried at 60 °C for 6 h.

Transformation of $Co(OH)_2$ Nanosheets into Nanoporous Hollow Co_3S_4 Nanosheets. In a typical chemical transformation procedure, 4.5 mL of the $Co(OH)_2$ stock solution was added into 7.5 mL of aqueous solution containing thioacetamide (0.0423 g) under continuous stirring. After 20 min of vigorous agitation, the dispersion was transferred into a 20 mL Teflon-lined autoclave and maintained at 120 °C for 6 h. The black samples were collected and washed several times with water and ethanol, separately, and then dried at 60 °C for 6 h.

Synthesis of Nanoporous Hollow Cobalt Selenide Nanosheets. $Co(OH)_2$ precursors (0.1 mmol) were dispersed in 12 mL of deionized water to form a homogeneous solution under constant strong agitation. Then, 0.2 mmol Se powder and 0.6 mmol $NaBH_4$ were added into the dispersion above under constant stirring. The mixed solution was transferred into a 20 mL Teflon-lined autoclave and maintained at 180 °C for 15 h. The samples were collected and washed three times with ethanol and water, separately, and then dried at 60 °C for 6 h.

Synthesis of Nanoporous Hollow Cobalt Telluride Nanosheets. The procedure for the preparation of nanoporous hollow cobalt tellurides nanosheets is the same as that described above except that the Se powder was replaced by Te powder.

Synthesis of Cadmium Hydroxide ($Cd(OH)_2$) Nanosheets. The $Cd(OH)_2$ nanosheets were synthesized using the reported method.[69] In a typical procedure, 2 mmol of $Cd(CH_3COO)_2$ was dissolved in 30 mL of deionized water to form a dispersive solution at room temperature. Then, 1 mmol of sodium ethylene diamine tetraacetic acid was added to the mixed solution under magnetic stirring. After 20 min of constant stirring, the mixed solution was then transferred into a 50 mL Teflon-lined stainless-steel autoclave and kept at 200 °C for 12 h. After cooling to room temperature naturally, the samples were collected and washed three times with ethanol and water, separately, and then dried at 60 °C for 6 h.

Conversion of $Cd(OH)_2$ Nanosheets into Nanoporous Hollow CdS Nanosheets. For a typical synthesis, 0.5 mmol of $Cd(OH)_2$ nanosheets precursors was dispersed in 15 mL of ethylene glycol by sonication, and then 2.5 mmol thiourea was added to the mixed solution under stirring. After 20 min of constant stirring, the dispersion was transferred into a 20 mL Teflon-lined autoclave and heated at 200 °C for 12 h. After cooling to room temperature naturally, the black precipitates were separated from solution, and washed several times with deionized water and absolute ethanol, separately. Then, the products were dried at 60 °C for 6 h.

Synthesis of Nickel Hydroxide ($Ni(OH)_2$) Nanosheet-Based Microspheres. The $Ni(OH)_2$ nanosheet-based microspheres were prepared according to the reported reference.[24] In a typical procedure, 0.5 mmol of $NiSO_4 \cdot 6H_2O$ was dissolved in 10 mL deionized water to form a green solution, and then 1.5 mL of 2 M ammonia was added to form an opaque dispersion under stirring. After 20 min of constant stirring, the dispersion was transferred into a 20 mL Teflon-lined autoclave and heated at 180 °C for 24 h. After cooling to room temperature naturally, the green precipitates were separated from the solution, and washed several times with deionized water and absolutely ethanol, separately. Then, the collected products were dried at 60 °C for 6 h.

Conversion of $Ni(OH)_2$ Nanosheets into Nanoporous Hollow NiS Nanosheets. For a typical synthesis, 10 mg of the free-flowing dry $Ni(OH)_2$ nanosheet-based microspheres precursors was dispersed in 12 mL of deionized water by sonication, and then 0.085 mg of thioacetamide was added to the mixed solution under stirring. After 20 min of constant stirring, the dispersion was transferred into a 20 mL Teflon-lined autoclave and heated at 120 °C for 6 h. After cooling to room temperature naturally, the black precipitates were separated from solution, and washed several times with deionized water and absolutely ethanol, separately. Then, the collected products were dried at 60 °C for 6 h.

Preparation of Solid Cobalt Sulfide Nanosheets. In a typical procedure, $Co(NO_3)_2 \cdot 6H_2O$ (0.1091 g, 0.375 mmol) was dissolved into 15 mL of deionized water to form a pink solution at room temperature. Then, 0.375 mL of triethylamine was added dropwise to the mixed solution under magnetic stirring, and the solution immediately turned dark blue. Next, 14.625 mL of aqueous solution containing thioacetamide (0.282 g) was added again to reach a total volume of 30 mL. The mixed solution was then transferred into a 50 mL Teflon-lined stainless-steel autoclave and kept at 120 °C for 6 h. After cooling to room temperature naturally, the black precipitates were separated from solution and washed several times with deionized water and absolutely ethanol, separately. Then, the collected products were dried at 60 °C for 6 h.

Electrochemical Measurements. All electrochemical measurements were performed using an electrochemical workstation (CHI 660D, CH Instruments, Austin, TX). Pt wire and mercury–mercury oxide (Hg/HgO, 1 M KOH) were used as counter and reference electrodes, respectively. A glass carbon electrode decorated with catalyst samples was used as the working electrode. For a typical making procedure for the working electrode, 4 mg of catalyst samples was dispersed in 1 mL of 3:1 (v/v) water–ethanol mixed solvent with 40 μL of 5 wt %

Nafion solution, then the mixture was ultrasonicated for at least 30 min to generate a homogeneous ink. Then, 5 μL of the catalyst ink (containing about 20 μg of catalysts) was loaded onto a glassy carbon electrode of 3 mm in diameter (loading ~0.283 mg/cm^2). Finally, the as-prepared catalyst film was dried at room temperature. Before the electrochemical measurement, the electrolyte (0.1 M KOH) was degassed by bubbling argon for 30 min. The polarization curves were obtained by sweeping the potential from −0.2 to 0.9 V *vs* Hg/HgO at room temperature, with a sweep rate of 10 mV s^{-1}. The electrochemical impedance spectroscopy (EIS) measurements were carried out in the same configuration at η = 0.6 V from 10^6 to 0.02 Hz with an AC amplitude of 5 mV. All the plots were corrected with compensated cell resistance (*iR*).

Characterization. The scanning electron microscopy (SEM) images and Energy-dispersive X-ray spectroscopic (EDS) analysis were taken with a Hitachi S-4800 scanning electron microscope (SEM, 5 kV) equipped with the *Thermo Scientific* energy-dispersion X-ray fluorescence analyzer. Transmission electron microscopy (TEM), higher-magnification transmission electron microscopy (HRTEM) and EDS line-scan elemental distributions were carried out with JEOL JEM-2100F system equipped with the EDAX Genesis XM2. For all EDS point-scan and line−scan data, Co L, Cd L and S K spectra were used. Electron energy loss spectroscopy (EELS) elemental distribution images were obtained with FEI Tecnai G^{2}F20 system equipped with GIF 863 Tridiem (Gatan). Specimens for TEM and HRTEM measurements were prepared *via* dropcasting a droplet of ethanol suspension onto a copper grid, coated with a thin layer of amorphous porous carbon film, and allowed to dry in air. The X-ray diffraction patterns (XRD) of the products were recorded with a PANalytical X'Pert PRO X-ray diffractometer with Co Kα radiation (λ = 1.78897 nm) at 40 kV and 40 mA. Then, the data were converted into corresponding Cu Kα radiation. The surface area and pore size distributions of the synthesized materials were determined by nitrogen physisorption by a NOVA 2200e system. The surface area was calculated using the Brunauer−Emmett−Teller method. Pore size distributions were calculated using the Barrett−Joyner−Halenda method from the desorption branch. X-ray photoelectron spectroscopy (XPS) measurements were carried out with a spectrometer having Al Kα radiation (PHI5000VersaProbe). The binding energy was calibrated with the C 1s position of contaminant carbon in the vacuum chamber of the XPS instrument (284.8 eV).

Conflict of Interest: The authors declare no competing financial interest.

Acknowledgment. This work was financially supported by the National Natural Science Foundation of China (No. 21422104 and No. 21373149) and the Innovation Foundation of Tianjin University. We acknowledge Dr. Xue Qin for helpful discussion on the electrochemical impedance data.

Supporting Information Available: This file contains additional Figures S1−S18, their captions, and supplementary discussions. This material is available free of charge *via* the Internet at http://pubs.acs.org.

REFERENCES AND NOTES

1. Zheng, N.; Bu, X.; Feng, P. Synthetic Design of Crystalline Inorganic Chalcogenides Exhibiting Fast-Ion Conductivity. *Nature* **2003**, *426*, 428–432.
2. Santra, P. K.; Kamat, P. V. Tandem-Layered Quantum Dot Solar Cells: Tuning the Photovoltaic Response with Luminescent Ternary Cadmium Chalcogenides. *J. Am. Chem. Soc.* **2013**, *135*, 877–885.
3. Gao, M.-R.; Xu, Y.-F.; Jiang, J.; Yu, S.-H. Nanostructured Metal Chalcogenides: Synthesis, Modification, and Applications in Energy Conversion and Storage Devices. *Chem. Soc. Rev.* **2013**, *42*, 2986–3017.
4. Zhou, J.; Tian, G.; Chen, Y.; Meng, X.; Shi, Y.; Cao, X.; Pan, K.; Fu, H. *In Situ* Controlled Growth of $ZnIn_2S_4$ Nanosheets on Reduced Graphene Oxide for Enhanced Photocatalytic Hydrogen Production Performance. *Chem. Commun.* **2013**, *49*, 2237–2239.
5. Zhang, J.; Qi, L.; Ran, J.; Yu, J.; Qiao, S. Z. Ternary NiS/$Zn_xCd_{1-x}S$/Reduced Graphene Oxide Nanocomposites for Enhanced Solar Photocatalytic H_2-Production Activity. *Adv. Energy Mater.* **2014**, *4*, 1301925.
6. Buck, M. R.; Schaak, R. E. Emerging Strategies for the Total Synthesis of Inorganic Nanostructures. *Angew. Chem., Int. Ed.* **2013**, *52*, 6154–6178.
7. Gao, M.-R.; Jiang, J.; Yu, S.-H. Solution-Based Synthesis and Design of Late Transition Metal Chalcogenide Materials for Oxygen Reduction Reaction (ORR). *Small* **2012**, *8*, 13–27.
8. Gao, M.-R.; Lin, Z.-Y.; Jiang, J.; Yao, H.-B.; Lu, Y.-M.; Gao, Q.; Yao, W.-T.; Yu, S.-H. Selective Synthesis of Fe_7Se_8 Polyhedra with Exposed High-Index Facets and Fe_7Se_8 Nanorods by a Solvothermal Process in a Binary Solution and Their Collective Intrinsic Properties. *Chem.—Eur. J.* **2011**, *17*, 5068–5075.
9. Gao, M.-R.; Lin, Z.-Y.; Zhuang, T.-T.; Jiang, J.; Xu, Y.-F.; Zheng, Y.-R.; Yu, S.-H. Mixed-Solution Synthesis of Sea Urchin-Like NiSe Nanofiber Assemblies as Economical Pt-Free Catalysts for Electrochemical H_2 Production. *J. Mater. Chem.* **2012**, *22*, 13662–13668.
10. Jayaprakash, N.; Shen, J.; Moganty, S. S.; Corona, A.; Archer, L. A. Porous Hollow Carbon@Sulfur Composites for High-Power Lithium-Sulfur Batteries. *Angew. Chem., Int. Ed.* **2011**, *50*, 5904–5908.
11. Xu, Y.; Zhang, B. Recent Advances in Porous Pt-Based Nanostructures: Synthesis and Electrochemical Applications. *Chem. Soc. Rev.* **2014**, *43*, 2439–2450.
12. Skorb, E. V.; Andreeva, D. V.; Möhwald, H. Generation of a Porous Luminescent Structure through Ultrasonically Induced Pathways of Silicon Modification. *Angew. Chem., Int. Ed.* **2012**, *51*, 5138–5142.
13. Bao, N.; Shen, L.; Takata, T.; Domen, K. Self-Templated Synthesis of Nanoporous CdS Nanostructures for Highly Efficient Photocatalytic Hydrogen Production under Visible Light. *Chem. Mater.* **2007**, *20*, 110–117.
14. Lai, X.; Halpert, J. E.; Wang, D. Recent Advances in Micro-/nano-structured Hollow Spheres for Energy Applications: From Simple to Complex Systems. *Energy Environ. Sci.* **2012**, *5*, 5604–5618.
15. Yuan, C.; Wu, H. B.; Xie, Y.; Lou, X. W. Mixed Transition-Metal Oxides: Design, Synthesis, and Energy-Related Applications. *Angew. Chem., Int. Ed.* **2014**, *53*, 1488–1504.
16. Liu, J.; Xue, D. Thermal Oxidation Strategy towards Porous Metal Oxide Hollow Architectures. *Adv. Mater.* **2008**, *20*, 2622–2627.
17. Moon, G. D.; Joo, J. B.; Dahl, M.; Jung, H.; Yin, Y. Nitridation and Layered Assembly of Hollow TiO_2 Shells for Electrochemical Energy Storage. *Adv. Funct. Mater.* **2014**, *24*, 848–856.
18. Nethravathi, C.; Rajamathi, C. R.; Rajamathi, M.; Wang, X.; Gautam, U. K.; Golberg, D.; Bando, Y. Cobalt Hydroxide/Oxide Hexagonal Ring-Graphene Hybrids through Chemical Etching of Metal Hydroxide Platelets by Graphene Oxide: Energy Storage Applications. *ACS Nano* **2014**, *8*, 2755–2765.
19. Hu, P.; Pramana, S. S.; Cao, S.; Ngaw, C. K.; Lin, J.; Loo, S. C. J.; Tan, T. T. Y. Ion-Induced Synthesis of Uniform Single-Crystalline Sulphide-Based Quaternary-Alloy Hexagonal Nanorings for Highly Efficient Photocatalytic Hydrogen Evolution. *Adv. Mater.* **2013**, *25*, 2567–2572.
20. Osada, M.; Sasaki, T. Two-Dimensional Dielectric Nanosheets: Novel Nanoelectronics from Nanocrystal Building Blocks. *Adv. Mater.* **2012**, *24*, 210–228.
21. Yin, Y.; Erdonmez, C. K.; Cabot, A.; Hughes, S.; Alivisatos, A. P. Colloidal Synthesis of Hollow Cobalt Sulfide Nanocrystals. *Adv. Funct. Mater.* **2006**, *16*, 1389–1399.
22. Wang, Z.; Pan, L.; Hu, H.; Zhao, S. Co_9S_8 Nanotubes Synthesized on the Basis of Nanoscale Kirkendall Effect and Their Magnetic and Electrochemical Properties. *CrystEngComm* **2010**, *12*, 1899–1904.
23. Wu, X. J.; Huang, X.; Liu, J.; Li, H.; Yang, J.; Li, B.; Huang, W.; Zhang, H. Two-Dimensional CuSe Nanosheets with Microscale Lateral Size: Synthesis and Template-Assisted Phase

Transformation. *Angew. Chem., Int. Ed.* **2014**, *53*, 5083–5087.
24. Liu, Q.; Jin, J.; Zhang, J. $NiCo_2S_4$@graphene as a Bifunctional Electrocatalyst for Oxygen Reduction and Evolution Reactions. *ACS Appl. Mater. Interfaces* **2013**, *5*, 5002–5008.
25. Jeong, S.; Yoo, D.; Jang, J.-t.; Kim, M.; Cheon, J. Well-Defined Colloidal 2D Layered Transition-Metal Chalcogenide Nanocrystals *via* Generalized Synthetic Protocols. *J. Am. Chem. Soc.* **2012**, *134*, 18233–18236.
26. Son, D. H.; Hughes, S. M.; Yin, Y.; Alivisatos, A. P. Cation Exchange Reactions in Ionic Nanocrystals. *Science* **2004**, *306*, 1009–1012.
27. Moon, G. D.; Ko, S.; Xia, Y.; Jeong, U. Chemical Transformations in Ultrathin Chalcogenide Nanowires. *ACS Nano* **2010**, *4*, 2307–2319.
28. Li, H.; Brescia, R.; Povia, M.; Prato, M.; Bertoni, G.; Manna, L.; Moreels, I. Synthesis of Uniform Disk-shaped Copper Telluride Nanocrystals and Cation Exchange to Cadmium Telluride Quantum Disks with Stable Red Emission. *J. Am. Chem. Soc.* **2013**, *135*, 12270–12278.
29. Li, H.; Brescia, R.; Krahne, R.; Bertoni, G.; Alcocer, M. J.; D'Andrea, C.; Scotognella, F.; Tassone, F.; Zanella, M.; De Giorgi, M.; Manna, L. Blue-UV-Emitting ZnSe(Dot)/ZnS(Rod) Core/shell Nanocrystals Prepared from CdSe/CdS Nanocrystals by Sequential Cation Exchange. *ACS Nano* **2012**, *6*, 1637–1647.
30. Sines, I. T.; Vaughn, D. D.; Biacchi, A. J.; Kingsley, C. E.; Popczun, E. J.; Schaak, R. E. Engineering Porosity into Single-Crystal Colloidal Nanosheets Using Epitaxial Nucleation and Chalcogenide Anion Exchange Reactions: The Conversion of SnSe to SnTe. *Chem. Mater.* **2012**, *24*, 3088–3093.
31. Beberwyck, B. J.; Alivisatos, A. P. Ion Exchange Synthesis of III-V Nanocrystals. *J. Am. Chem. Soc.* **2012**, *134*, 19977–19980.
32. Rivest, J. B.; Jain, P. K. Cation Exchange on the Nanoscale: An Emerging Technique for New Material Synthesis, Device Fabrication, and Chemical Sensing. *Chem. Soc. Rev.* **2013**, *42*, 89–96.
33. Gupta, S.; Kershaw, S. V.; Rogach, A. L. Ion Exchange in Colloidal Nanocrystals. *Adv. Mater.* **2013**, *25*, 6923–6944.
34. Dawood, F.; Schaak, R. E. ZnO-Templated Synthesis of Wurtzite-Type ZnS and ZnSe Nanoparticles. *J. Am. Chem. Soc.* **2008**, *131*, 424–425.
35. Yao, Q.; Arachchige, I. U.; Brock, S. L. Expanding the Repertoire of Chalcogenide Nanocrystal Networks: Ag_2Se Gels and Aerogels by Cation Exchange Reactions. *J. Am. Chem. Soc.* **2009**, *131*, 2800–2801.
36. Yu, Y.; Yin, X.; Kvit, A.; Wang, X. Evolution of Hollow TiO_2 Nanostructures *via* the Kirkendall Effect Driven by Cation Exchange with Enhanced Photoelectrochemical Performance. *Nano Lett.* **2014**, *14*, 2528–2535.
37. Zhang, B.; Jung, Y.; Chung, H.-S.; Vugt, L. V.; Agarwal, R. Nanowire Transformation by Size-Dependent Cation Exchange Reactions. *Nano Lett.* **2009**, *10*, 149–155.
38. Yu, Y.; Zhang, J.; Wu, X.; Zhao, W.; Zhang, B. Nanoporous Single-Crystal-Like $Cd_xZn_{1-x}S$ Nanosheets Fabricated by the Cation-Exchange Reaction of Inorganic-Organic Hybrid ZnS-Amine with Cadmium Ions. *Angew. Chem., Int. Ed.* **2012**, *51*, 897–900.
39. Zhuo, S.; Xu, Y.; Zhao, W.; Zhang, J.; Zhang, B. Hierarchical Nanosheet-Based MoS_2 Nanotubes Fabricated by an Anion-Exchange Reaction of MoO_3-Amine Hybrid Nanowires. *Angew. Chem., Int. Ed.* **2013**, *52*, 8602–8606.
40. Wang, H.; Liang, Y.; Li, Y.; Dai, H. $Co_{1-x}S$-Graphene Hybrid: A High-Performance Metal Chalcogenide Electrocatalyst for Oxygen Reduction. *Angew. Chem., Int. Ed.* **2011**, *50*, 10969–10972.
41. Tran, P. D.; Chiam, S. Y.; Boix, P. P.; Ren, Y.; Pramana, S. S.; Fize, J.; Artero, V.; Barber, J. Novel Cobalt/Nickel-Tungsten-Sulfide Catalysts for Electrocatalytic Hydrogen Generation from Water. *Energy Environ. Sci.* **2013**, *6*, 2452–2459.
42. Sun, Y.; Liu, C.; Grauer, D. C.; Yano, J.; Long, J. R.; Yang, P.; Chang, C. J. Electrodeposited Cobalt-Sulfide Catalyst for Electrochemical and Photoelectrochemical Hydrogen Generation from Water. *J. Am. Chem. Soc.* **2013**, *135*, 17699–17702.
43. Moon, G. D.; Ko, S.; Min, Y.; Zeng, J.; Xia, Y.; Jeong, U. Chemical Transformations of Nanostructured Materials. *Nano Today* **2011**, *6*, 186–203.
44. Yan, C.; Rosei, F. Hollow Micro/nanostructured Materials Prepared by Ion Exchange Synthesis and Their Potential Applications. *New J. Chem.* **2014**, *38*, 1883–1904.
45. Liu, X.; Yi, R.; Zhang, N.; Shi, R.; Li, X.; Qiu, G. Cobalt Hydroxide Nanosheets and Their Thermal Decomposition to Cobalt Oxide Nanorings. *Chem.—Asian J.* **2008**, *3*, 732–738.
46. Liu, Q.; Zhang, J. A General and Controllable Synthesis of Co_mS_n(Co_9S_8, Co_3S_4, and $Co_{1-x}S$) Hierarchical Microspheres with Homogeneous Phases. *CrystEngComm* **2013**, *15*, 5087–5092.
47. Yin, Y.; Rioux, R. M.; Erdonmez, C. K.; Hughes, S.; Somorjai, G. A.; Alivisatos, A. P. Formation of Hollow Nanocrystals through the Nanoscale Kirkendall Effect. *Science* **2004**, *304*, 711–714.
48. González, E.; Arbiol, J.; Puntes, V. F. Carving at the Nanoscale: Sequential Galvanic Exchange and Kirkendall Growth at Room Temperature. *Science* **2011**, *334*, 1377–1380.
49. Fan, H. J.; Gösele, U.; Zacharias, M. Formation of Nanotubes and Hollow Nanoparticles Based on Kirkendall and Diffusion Processes: a Review. *Small* **2007**, *3*, 1660–1671.
50. Liang, X.; Wang, X.; Zhuang, Y.; Xu, B.; Kuang, S.; Li, Y. Formation of CeO_2-ZrO_2 Solid Solution Nanocages with Controllable Structures *via* Kirkendall Effect. *J. Am. Chem. Soc.* **2008**, *130*, 2736–2737.
51. Yu, L.; Zhang, L.; Wu, H. B.; Lou, X. W. D. Formation of $Ni_xCo_{3-x}S_4$ Hollow Nanoprisms with Enhanced Pseudocapacitive Properties. *Angew. Chem., Int. Ed.* **2014**, *53*, 3711–3714.
52. Li, R.; Luo, Z.; Papadimitrakopoulos, F. Redox-assisted Asymmetric Ostwald Ripening of CdSe Dots to Rods. *J. Am. Chem. Soc.* **2006**, *128*, 6280–6281.
53. Saruyama, M.; Kanehara, M.; Teranishi, T. Drastic Structural Transformation of Cadmium Chalcogenide Nanoparticles Using Chloride Ions and Surfactants. *J. Am. Chem. Soc.* **2010**, *132*, 3280–3282.
54. ChunáZeng, H. Synthesis of Complex Nanomaterials *via* Ostwald Ripening. *J. Mater. Chem. A* **2014**, *2*, 4843–4851.
55. Li, L.; Cao, R.; Wang, Z.; Li, J.; Qi, L. Template Synthesis of Hierarchical Bi_2E_3 (E = S, Se, Te) Core-Shell Microspheres and Their Electrochemical and Photoresponsive Properties. *J. Mater. Chem. C* **2009**, *113*, 18075–18081.
56. Oyler, K. D.; Ke, X.; Sines, I. T.; Schiffer, P.; Schaak, R. E. Chemical Synthesis of Two-Dimensional Iron Chalcogenide Nanosheets: FeSe, FeTe, Fe(Se,Te), and $FeTe_2$. *Chem. Mater.* **2009**, *21*, 3655–3661.
57. Gao, J.; Zhang, B.; Zhang, X.; Xu, B. Magnetic-Dipolar-Interaction-Induced Self-Assembly Affords Wires of Hollow Nanocrystals of Cobalt Selenide. *Angew. Chem., Int. Ed.* **2006**, *45*, 1220–1223.
58. Van der Heide, H.; Hemmel, R.; Van Bruggen, C. F.; Haas, C. X-Ray Photodectron Spectra of 3d Transition Metal Pyrites. *J. Solid State Chem.* **1980**, *1*, 17–25.
59. Zhou, W.; Wu, X.-J.; Cao, X.; Huang, X.; Tan, C.; Tian, J.; Liu, H.; Wang, J.; Zhang, H. Ni_3S_2 Nanorods/Ni Foam Composite Electrode with Low Overpotential for Electrocatalytic Oxygen Evolution. *Energy Environ. Sci.* **2013**, *6*, 2921–2924.
60. Zhou, W.; Cao, X.; Zeng, Z.; Shi, W.; Zhu, Y.; Yan, Q.; Liu, H.; Wang, J.; Zhang, H. One-Step Synthesis of Ni_3S_2 Nanorod@$Ni(OH)_2$ Nanosheet Core-Shell Nanostructures on a Three-Dimensional Graphene Network for High-performance Supercapacitors. *Energy Environ. Sci.* **2013**, *6*, 2216–2221.
61. Gao, M.-R.; Xu, Y.-F.; Jiang, J.; Zheng, Y.-R.; Yu, S.-H. Water Oxidation Electrocatalyzed by an Efficient Mn_3O_4/$CoSe_2$ Nanocomposite. *J. Am. Chem. Soc.* **2012**, *134*, 2930–2933.
62. Gao, M.-R.; Cao, X.; Gao, Q.; Xu, Y.-F.; Zheng, Y.-R.; Jiang, J.; Yu, S.-H. Nitrogen-Doped Graphene Supported $CoSe_2$ Nanobelt Composite Catalyst for Efficient Water Oxidation. *ACS Nano* **2014**, *8*, 3970–3978.

63. Xu, Y.-F.; Gao, M.-R.; Zheng, Y.-R.; Jiang, J.; Yu, S.-H. Nickel/Nickel(II) Oxide Nanoparticles Anchored onto Cobalt(IV) Diselenide Nanobelts for the Electrochemical Production of Hydrogen. *Angew. Chem., Int. Ed.* **2013**, *52*, 8546–8550.
64. Gao, M.; Sheng, W.; Zhuang, Z.; Fang, Q.; Gu, S.; Jiang, J.; Yan, Y. Efficient Water Oxidation Using Nanostructured Alpha-Nickel-Hydroxide as an Electrocatalyst. *J. Am. Chem. Soc.* **2014**, *136*, 7077–7084.
65. Xia, X.-h.; Tu, J.-p.; Wang, X.-l.; Gu, C.-d.; Zhao, X.-b. Hierarchically Porous NiO Film Grown by Chemical Bath Deposition *via* a Colloidal Crystal Template as an Electrochemical Pseudocapacitor Material. *J. Mater. Chem.* **2011**, *21*, 671–679.
66. Lu, Z.; Xu, W.; Zhu, W.; Yang, Q.; Lei, X.; Liu, J.; Li, Y.; Sun, X.; Duan, X. Three-Dimensional NiFe Layered Double Hydroxide Film for High-efficiency Oxygen Evolution Reaction. *Chem. Commun.* **2014**, *50*, 6479–6482.
67. Xia, X.; Tu, J.; Zhang, Y.; Wang, X.; Gu, C.; Zhao, X.-b.; Fan, H. J. High-Quality Metal Oxide Core/Shell Nanowire Arrays on Conductive Substrates for Electrochemical Energy Storage. *ACS Nano* **2012**, *6*, 5531–5538.
68. Cho, S.; Fowler, D. E.; Miller, E. C.; Cronin, J. S.; Poeppelmeier, K. R.; Barnett, S. A. Fe-substituted $SrTiO_{3-\delta}$-$Ce_{0.9}Gd_{0.1}O_2$ Composite Anodes for Solid Oxide Fuel Cells. *Energy Environ. Sci.* **2013**, *6*, 1850–1857.
69. Jiang, H.; Hu, J.; Li, C.; Gu, F.; Ma, J. Large-Scale, Uniform, Single-Crystalline $Cd(OH)_2$ Hexagonal Platelets for Cd-Based Functional Applications. *CrystEngComm* **2010**, *12*, 1726–1729.